Matter

CellPress
OPEN ACCESS

Article

Designing nanostructure exsolution-self-assembly in a complex concentrated oxide

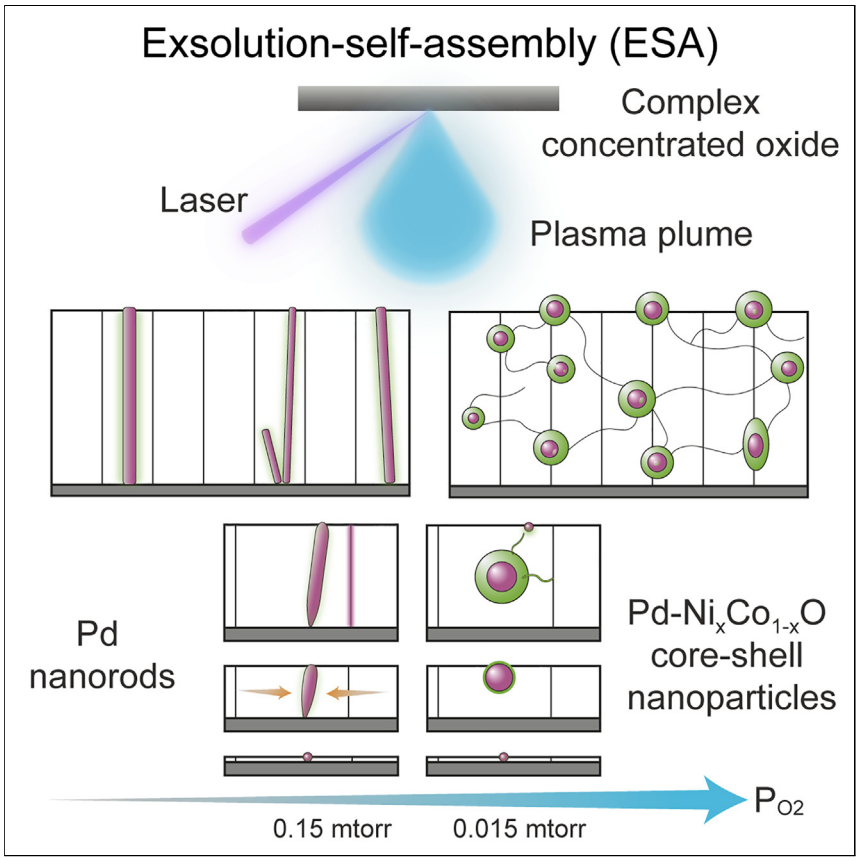

A new exsolution-self-assembly (ESA) approach was demonstrated during thin film growth, combining aspects of immiscibility-driven one-step self-assembly with defect-interaction-driven two-step exsolution to yield novel vertically aligned nanostructures and particle-in-matrix nanocomposites. The one-step ESA synthesis is applied to a model complex concentrated oxide, an emerging class of materials including high-entropy and entropy-stabilized oxides, whose ability to stabilize five or more cations in a single crystal structure provides a combinatorial space for new materials with broad electrochemical and information storage applications.

Huiming Guo, Christopher Mead, Marquez Balingit, ..., Kandis Leslie Gilliard-AbdulAziz, Lincoln J. Lauhon, William J. Bowman

will.bowman@uci.edu

Highlights

Tunable nanostructures in a complex concentrated oxide by exsolution-self-assembly

An approach to direct the evolution of nanoparticles and nanorods via oxygen pressure

Cation reducibility predicts nanostructure chemical composition, tailoring growth

Mass transport through extended defects governs local morphology

Benchmark
First qualification/assessment of material properties and/or performance

Guo et al., Matter 7, 1–16
March 6, 2024
https://doi.org/10.1016/j.matt.2023.12.012

Please cite this article in press as: Guo et al., Designing nanostructure exsolution-self-assembly in a complex concentrated oxide, Matter (2023), https://doi.org/10.1016/j.matt.2023.12.012

Matter

CellPress
OPEN ACCESS

Article

Designing nanostructure exsolution-self-assembly in a complex concentrated oxide

Huiming Guo,[1] Christopher Mead,[2] Marquez Balingit,[1] Soham Shah,[3] Xin Wang,[1] Mingjie Xu,[4] Ich Tran,[4] Toshihiro Aoki,[4] Jack D. Samaniego,[1] Kandis Leslie Gilliard-AbdulAziz,[3] Lincoln J. Lauhon,[2] and William J. Bowman[1,4,5,*]

SUMMARY

Complex concentrated oxides (CCOs) are an emerging material class that includes high-entropy and entropy-stabilized oxides whose properties stem from disorder-induced electronic structure and chemistry caused by stabilizing solid solutions of >5 cations. Integrating CCOs into composites will expand material design beyond the single-phase paradigm. We demonstrate tunable CCO-derived nanostructures by a simple method: exsolution-self-assembly (ESA), a one-step approach to direct the evolution of nanoparticles and nanorods in nanocomposites. We have developed a fundamental understanding of driving forces and formation mechanisms in CCOs using atomic-scale probes, which reveal that ESA can be directed using Ellingham's model of cation reducibility in a model CCO perovskite $LaFe_{0.7}Ni_{0.1}Co_{0.1}Pd_{0.05}Ru_{0.05}O_{3-\delta}$. This approach enables tailored growth of multielement nanorod and nanoparticle composite structures whose formation is correlated with electronic conductivity that exceeds 0.1 S/cm at room temperature. Given the vast combinatorial space of CCOs, ESA is expected to be highly extensible via the integration of various compositions and crystal structures.

INTRODUCTION

Recently, unprecedented materials have been realized by stabilizing a relatively large number (>5) of cations in solid solution, wherein phase stability is enhanced or provided by high configurational entropy associated with compositional complexity.[1] This emerging class of complex concentrated oxides (CCOs)—including high-entropy oxides (HEOs) with elevated configurational entropy and entropy-stabilized oxides (ESOs), which are unequivocally stabilized by entropy[2]—provides a novel tuning route beyond conventional chemical composition to improve material properties by controlling the distributions of lattice disorder, bond energy, defect formation, and cation multivalency.[3,4] Although research on CCOs/HEOs/ESOs has focused mainly on single-phase materials, our very recent work shows that ESO phase separation into a composite provides novel control over electrical transport mechanisms by directing ionic and electronic current through the different composite phases, highlighting the potential of composite micro- and nanostructures[5,6] to finely tailor the properties of these emerging materials and broaden their potential applications.

Exsolution[7,8] is a multistep synthesis understood by considering atomistic interactions between charged point defects. A reducible oxide is exposed to a reducing

PROGRESS AND POTENTIAL

Complex concentrated oxides (CCOs) include high-entropy and entropy-stabilized oxides, whose ability to stabilize five or more cations in a single-crystal structure provides a vast design space for new materials. In a model CCO, we demonstrate exsolution-self-assembly (ESA), a highly extensible synthesis for diverse and exotic nanocomposites. ESA combines the benefits of reducibility-controlled metal cation exsolution with the spontaneity of immiscibility-driven self-assembly to produce intricate tailorable nanostructures in a single synthetic step. Application of ESA to CCOs and advanced entropy-designed chemical compositions and crystal structures will yield multidimensional and multielement nanostructures for next-generation electrochemical, electronic, and information storage devices. The synthesis has the potential to create highly tunable nanocomposites that combine the properties and functions of emerging high-entropy materials with precisely designed embedded nanostructures.

Please cite this article in press as: Guo et al., Designing nanostructure exsolution-self-assembly in a complex concentrated oxide, Matter (2023), https://doi.org/10.1016/j.matt.2023.12.012

atmosphere, forming oxygen vacancies that electrostatically promote the accumulation of metal cations into nanoparticles anchored (i.e., partially submerged) in the surface of a material[9] and/or embedded (submerged) within the material.[10] Exsolution offers tunable and stable nanostructures, flexible material selection, and structure modulation of the oxide matrix,[11–14] but it requires relatively long treatment time at high temperature under reducing gases. Unlike exsolution, nanocomposite self-assembly occurs spontaneously in one step during thin film deposition by physical vapor deposition following one of two mechanisms: diffusion, nucleation, and growth for materials systems with limited miscibility, and (pseudo)spinodal decomposition for miscible materials.[15] Self-assembled nanostructures have final shape, size, spatial distribution, and crystallographic orientation relative to the matrix governed by free energy minimization.[5]

Here, we present the exsolution-self-assembly (ESA) method, whereby nanostructures form spontaneously from a miscible single-phase solid solution during film growth due to both immiscibility of the new nanophase in the matrix and atomistic interactions between point defects. We demonstrate tunable nanostructure growth in a CCO by ESA, which should provide improved synthetic control of nanoparticles and nanorods across a broader phase space than is currently possible.[16] We present a case study demonstrating simple access of different nanostructures via control of oxygen partial pressure (P_{O_2}) during pulsed laser deposition (PLD, Figure 1A). ESA using a CCO precursor enables novel multielement composite morphologies with finely tuned subphase chemical composition that are not possible by conventional exsolution or self-assembly independently. Moreover, the demonstrated fabrication method is shown to work on a variety of substrate materials with application potential in industrial semiconductors and electrochemical devices. By mapping the distribution of distinct subphase structure and chemistry with nanometer spatial resolution, we show that Ellingham's model of cation reducibility predicts nanostructure chemical composition, whereas mass transport via extended defects governs local morphology formation.[17,18] This is demonstrated in $LaFe_{0.7}Co_{0.1}Ni_{0.1}Ru_{0.05}Pd_{0.05}O_{3-\delta}$, a model CCO inspired by the $LaFeO_3$ perovskite, which has promising applications in solid oxide fuel/electrolysis cell electrodes, hydride batteries, supercapacitors,[19–21] gas sensors, electromechanical devices, (photo)electrocatalysis, and photovoltaics due to its abundance, nontoxicity, chemical stability, and direct band gap.[22,23] However, a key drawback of some $LaFeO_3$-based materials is sluggish electronic conductivity (<0.1 S/cm), weak sensing response, low catalytic selectivity, and poor charge separation that seriously restricts performance.[22,24] More important, the electronic conductivity of our nanocomposites exceeds 0.1 S/cm at room temperature, with transport correlated to nanostructure formation primarily through B-site cation (i.e., Ni and Co) mixed valency and site occupancy in the CCO matrix. Given the vast combinatorial space of CCOs, ESA is expected to be highly extensible through application to novel compositions and crystal structures, with the understanding presented here enabling one to take advantage of chemical complexity in a rational way.

RESULTS

To demonstrate the potential of ESA to access diverse nanocomposite microstructure with simple process variations, we varied the P_{O_2} during PLD to precisely tune the $V_O^{\cdot\cdot}$ concentration, which in turn controls cation exsolution and matrix decomposition (Figure 1M). At low P_{O_2}, $V_O^{\cdot\cdot}$ formation in the perovskite oxide destabilizes B-site cations, inducing exsolution and matrix decomposition. The orthorhombic/pseudocubic (121)/$(110)_c$ X-ray diffraction (XRD) peak of the CCO matrix shifts

[1]Department of Materials Science and Engineering, University of California Irvine, Irvine, CA 92697, USA

[2]Department of Materials Science and Engineering, Northwestern University, Evanston, IL 60208, USA

[3]Department of Chemical and Environmental Engineering, University of California Riverside, Riverside, CA 92521, USA

[4]Irvine Materials Research Institute (IMRI), University of California Irvine, Irvine, CA 92697, USA

[5]Lead contact

*Correspondence: will.bowman@uci.edu

https://doi.org/10.1016/j.matt.2023.12.012

Please cite this article in press as: Guo et al., Designing nanostructure exsolution-self-assembly in a complex concentrated oxide, Matter (2023), https://doi.org/10.1016/j.matt.2023.12.012

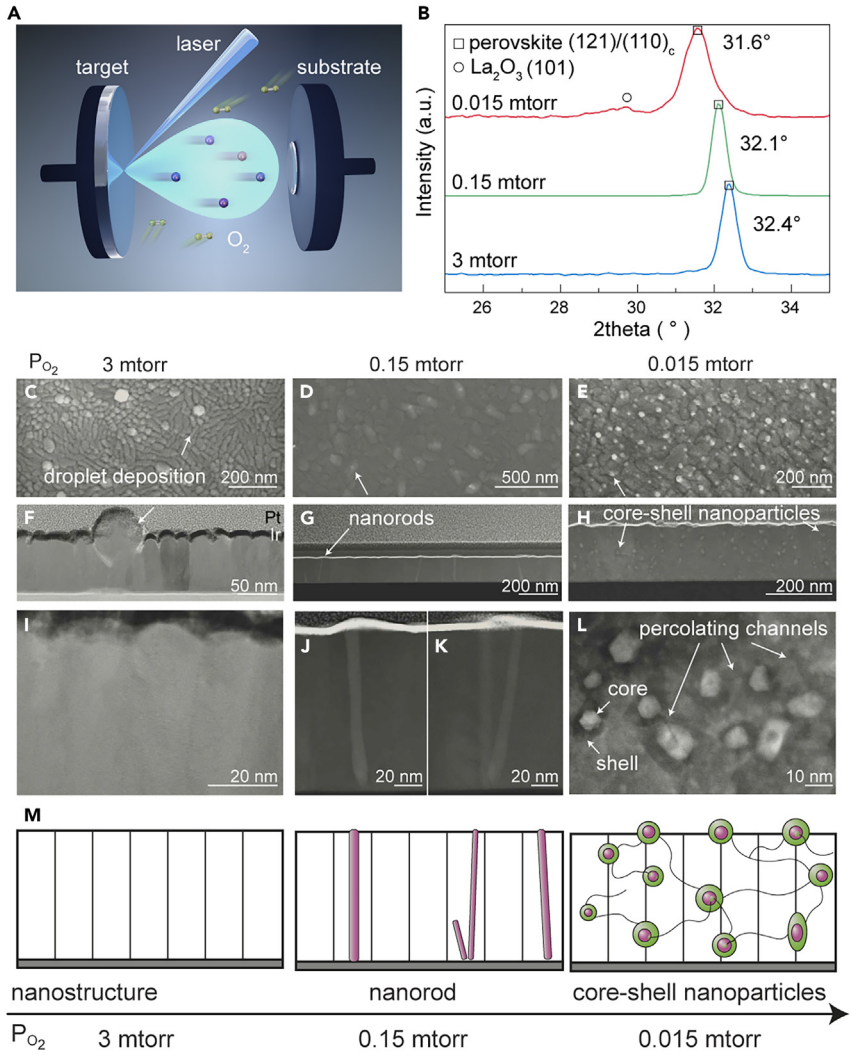

Figure 1. Tuning the morphology of exsolution-self-assembled nanostructures via P_{O_2}

(A) Depositing $LaFe_{0.7}Co_{0.1}Ni_{0.1}Ru_{0.05}Pd_{0.05}O_{3-\delta}$ thin films with PLD.

(B) XRD patterns of the perovskite thin films deposited at 3, 0.15,and 0.015 mTorr. Matrix diffraction peaks shift left with decreasing P_{O_2}, indicating that higher $V_O^{\cdot\cdot}$ content expands the unit cell.

(C–E) SEM secondary electron (SE) images of the films deposited at 3 (C), 0.15 (D), and 0.015 mTorr (E), showing top view of self-assembled nanophases.

(F and I) Low- (F) and high-magnification (I) STEM bright-field images of the film deposited at 3 mTorr, with no self-assembled phase observed.

(G, J, and K) Low- (G) and high-magnification (J and K) STEM HAADF images of the film deposited at 0.15 mTorr showing the cross-section of self-assembled nanophases. Self-assembled nanorods grow from the bottom of the thin film to the top surface.

(H and L) Low- (H) and high-magnification (L) STEM HAADF images of the film deposited at 0.015 mTorr. Self-assembled core-shell nanoparticles joined with percolating channels both embedded inside the perovskite matrix and exposed on thin film surface.

from 32.4° to 31.6° with decreasing P_{O_2} from 3 to 0.015 mTorr (Figures 1B, S1A, and S1B; Note S1), indicating unit cell expansion due to lower $V_O^{\cdot\cdot}$ formation energy in oxygen-deficient environments.[25,26] La_2O_3 (101) secondary phase peaks appear after deposition at 0.015 mTorr, illustrating that the perovskite structure collapses locally. Elevated $V_O^{\cdot\cdot}$ concentration with declining P_{O_2} was corroborated by tracking oxygen species by O1s X-ray photoelectron spectroscopy (XPS) in

Please cite this article in press as: Guo et al., Designing nanostructure exsolution-self-assembly in a complex concentrated oxide, Matter (2023), https://doi.org/10.1016/j.matt.2023.12.012

the film's top-most ~10 nm (Figures 6A and S2; Table S1; Note S2). When P_{O_2} = 3 mTorr, no self-assembled phases are observed (Figures 1C, 1F, and 1I). When P_{O_2} = 0.15 mTorr, nanorods form in the matrix (Figures 1G, 1J, and 1K), with an average width of 10 nm. Most grow from thin film bottom to the top surface continuously, with an average length of 120 nm. White dots in the scanning electron microscopy (SEM) top-view image (Figure 1D) are nanorod tips. When P_{O_2} = 0.015 mTorr, abundant and well-dispersed core-shell nanoparticles form, with sizes of 7–26 nm (average 19 nm; Figures S27 and S28; Note S16), high population density (332 μm^{-2}), and interconnected by percolating channels (Figures 1E, 1H, and 1L) similar to those reported in studies of two-step Fe exsolution.[11,27] In addition, similar phase composition and crystallographic textures are observed in films grown on amorphous and crystalline oxides and metals (Figures S1A–S1C; Note S1), suggesting the general applicability of this method to different device architectures.

The chemical heterogeneity associated with the composite microstructures was characterized using scanning transmission electron microscopy energy-dispersive X-ray spectroscopy (STEM EDS) and electron energy loss spectroscopy (EELS) (Figures 2 and S3; Note S3). At P_{O_2} = 3 mTorr, uniform elemental distribution (Figures 2A, 2D, 2G, 2J, 2M, 2P, S3A, and S3B) demonstrates that B-site cations remain stable in matrix, except Ru. At P_{O_2} = 0.15 mTorr, nanorods are Pd with subtle Ni and Co segregation at matrix–rod interfaces (Figures 2B, 2E, 2H, 2K, 2N, 2Q, S3C–S3F, and S7). At P_{O_2} = 0.015 mTorr, core-shell nanoparticles comprise Pd cores and $Ni_xCo_{1-x}O$ shells (Figures 2C, 2F, 2I, 2L, 2O, 2R, S3G, and S3H); La and Fe show nonuniform distribution in the surrounding matrix (Figure 2F), consistent with XRD detection of La_2O_3 (Figure 1B). All of the films show Ru surface segregation (Figures 2P and 2R), which atom probe tomography (APT) confirms (Figure S4). Surface accumulation of Ru at 3 mTorr reflects its greater tendency toward reducibility compared to Pd, in line with its weak metal–support interaction compared with Pd in $LaFeO_3$[28,29] (Note S4).

Nanophase identification, composition, and formation mechanism

To confirm that the Pd-containing nanorods were Pd metal and to understand the nanorod growth mechanism, atomic-resolution STEM high-angle annular dark field (HAADF) imaging and geometric phase analysis (GPA) were used to identify the nanorod crystal structure and map local strain in the matrix (Figures 3, S5, and S6). When viewing the perovskite matrix along the perovskite $[100]_c$ zone axis, the Pd metal nanorod lattice was directly visible in the [111] zone-axis orientation (Figures 3A–3C). To decipher the formation mechanism of the Pd nanorods, GPA was applied to Figure 3A to map the perovskite strain near the Pd nanorod (Figures 3D and 3E). The tensile in-plane lateral strain of the matrix is 10 times larger than the tensile out-of-plane vertical strain at the interface with the Pd nanorod (Figure 3F). The in-plane Pd lattice constant is compressed by 3.4% compared with standard Pd (Figure S6; Table S2), indicating that nanorod lateral growth is restricted by the matrix. The compressive stress contributes to the balance of forces/energies that defines the diameter of the Pd nanorod and thus the amount of laterally diffusing Pd that can be accommodated in each growth layer.[15] In addition, Pd nanorods grow inclined at/near grain boundaries (GBs) with Pd segregation (Figure 3G). It is hypothesized that Pd sourced from GBs creates nanorods inclined toward GBs (Figures 3H and 3I). Therefore, the growth of Pd is restricted by both the elastic energy and the availability of Pd in surrounding GBs (Figure 3J). Ni and Co segregation at the matrix–Pd nanorod interface, observed by STEM EDS (Figures 2H, 2K, and S7) may result from local tensile strain of the perovskite, which lowers the $V_O^{\cdot\cdot}$ formation

Please cite this article in press as: Guo et al., Designing nanostructure exsolution-self-assembly in a complex concentrated oxide, Matter (2023), https://doi.org/10.1016/j.matt.2023.12.012

CellPress
OPEN ACCESS

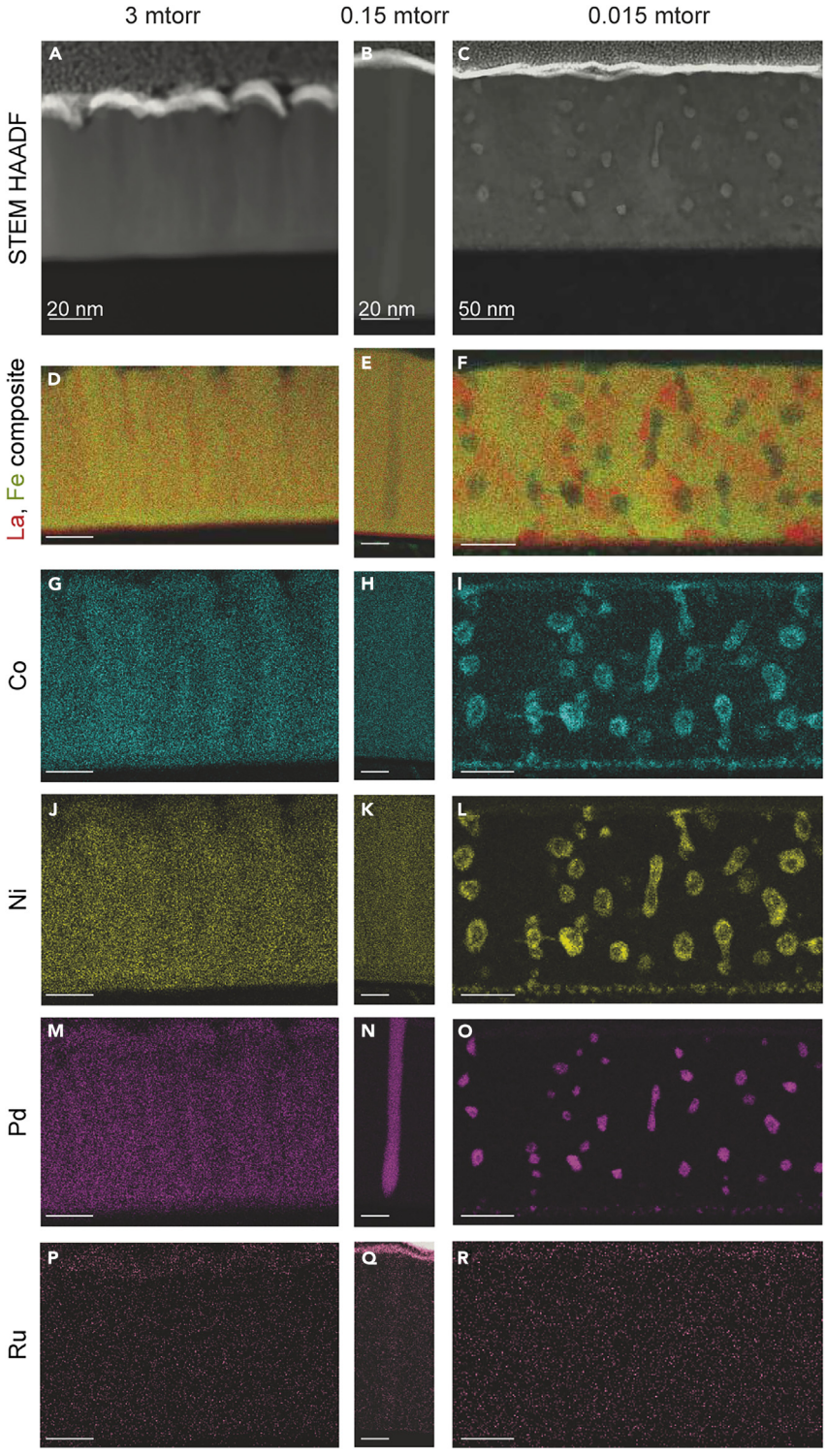

Figure 2. Elemental mapping of exsolution-self-assembled nanostructures tuned by P_{O_2}

(A–C) STEM HAADF images of the CCO-derived nanocomposite thin films.

(D–N) STEM EDS mapping of (D–F) La and Fe, (G–I) Co, (J–L) Ni, and (M and N) Pd.

(P–R) STEM EELS mapping of Ru.

Please cite this article in press as: Guo et al., Designing nanostructure exsolution-self-assembly in a complex concentrated oxide, Matter (2023), https://doi.org/10.1016/j.matt.2023.12.012

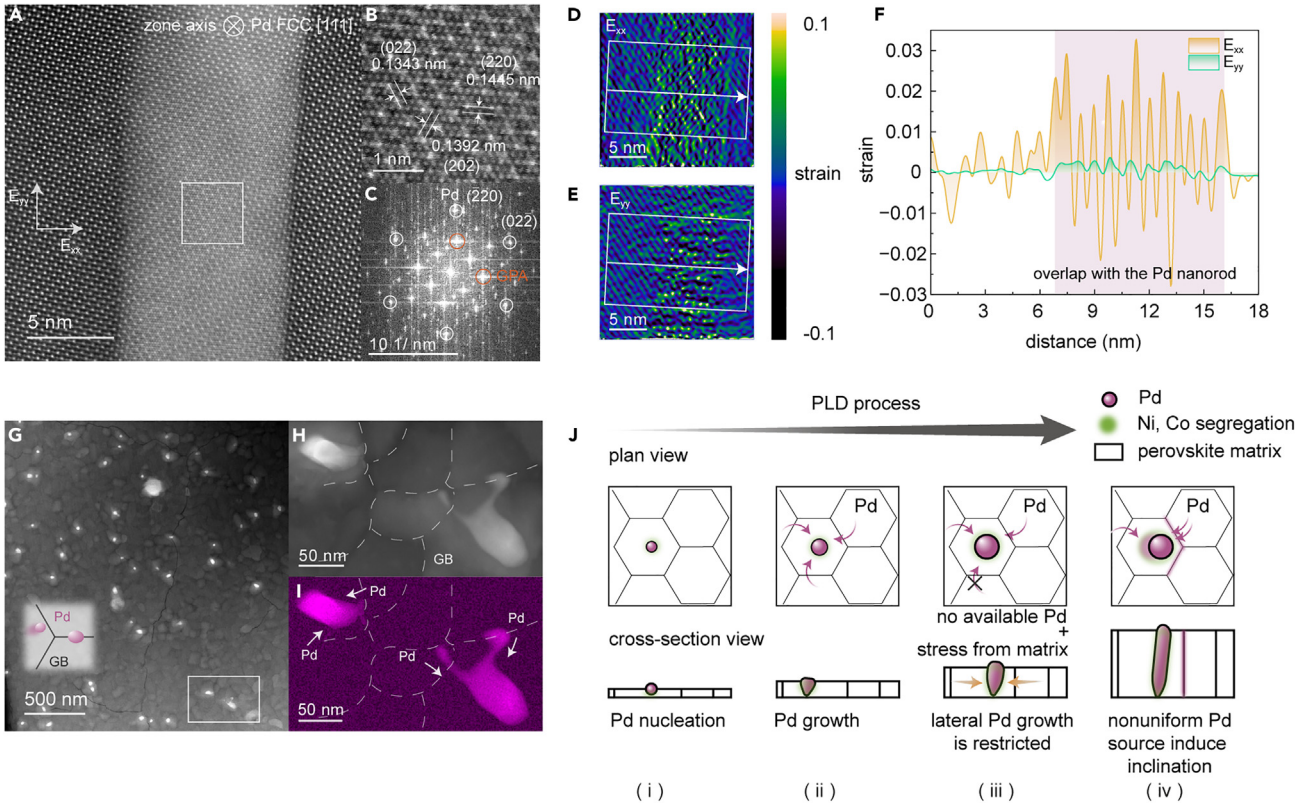

Figure 3. Phase identification and formation mechanism of exsolution-self-assembled Pd nanorods

(A–C) Cross-section STEM HAADF image of a Pd nanorod embedded in the perovskite matrix (A). Local magnified image of area marked in (A), showing Pd atom arrangement and Pd {220} plane spacing (B), and FFT pattern of (A) showing the Pd nanorod along the [111] zone axis and the matrix along the $[100]_c$ zone axis (C).

(D and E) Strain mapping of perovskite matrix in (A) along lateral in-plane direction (E_{xx}) (D) and vertical out-of-plane direction (E_{yy}) (E) via GPA. Directions of E_{xx} and E_{yy} are labeled in (A).

(F) Strain profile of the interface matrix with Pd nanorod along the direction marked in (D and E). E_{xx} shows tensile strain approximately 10 times higher than E_{yy} at the interface, indicating that compressive stress from perovskite matrix restricts growth of Pd nanorod in lateral direction.

(G–I) Plan -view STEM HAADF image of Pd nanorods embedded in the perovskite matrix (G), (H) is the local magnified image marked in (G), and corresponding EDS mapping of Pd (I). Plan-view observation shows the Pd nanorods are located at or close to GBs, and Pd nanorods show inclined growth as shown as the schematic inset in (G).

(J) Schematic illustration of mechanism of Pd nanorod growth. Pd nucleates at the beginning of PLD (i), then surrounding Pd diffuse to the nucleus to grow laterally and vertically (ii). The lateral growth of Pd is restricted by compressive stress from matrix and limited availability of Pd from the surroundings, forming Pd nanorods (iii). Nonuniform Pd sourcing from grains and GBs leads to inclined growth of Pd nanorods (iv).

energy[30] to reduce Ni^{3+} and Co^{3+} and accommodates the larger-radii Ni^{2+} and Co^{2+} species.

In the core-shell composites, self-assembled nanostructures were confirmed to be metal-oxide Pd-$Ni_xCo_{1-x}O$ core-shells using crystal structure and composition mapping by fast Fourier transform (FFT) analysis (Figures S9–S11), STEM EDS (Figures 4B, 4C, S9, and S10), and APT (Figures 5 and S26; Note S15). Representative core-shell nanoparticles and percolating channels connecting them are shown in Figure 4A and Note S8. Crystal structures of the perovskite matrix, nanoparticle core and rock salt shell, and La_2O_3 were resolved based on inverse FFT (IFFT) patterns (Figure S9F). FFT patterns of the core show FCC {111} and {200} with lattice parameters of Pd metal (Figure S9I). FFT patterns of the rock salt shell (Figure S9G) shows a lattice parameter of 4.192 Å, which is between NiO (4.177 Å) and CoO (4.261 Å).[31,32] Elemental mapping (Figures 4B, 4C, and S8B–S8D) is consistent with the FFT phase

Please cite this article in press as: Guo et al., Designing nanostructure exsolution-self-assembly in a complex concentrated oxide, Matter (2023), https://doi.org/10.1016/j.matt.2023.12.012

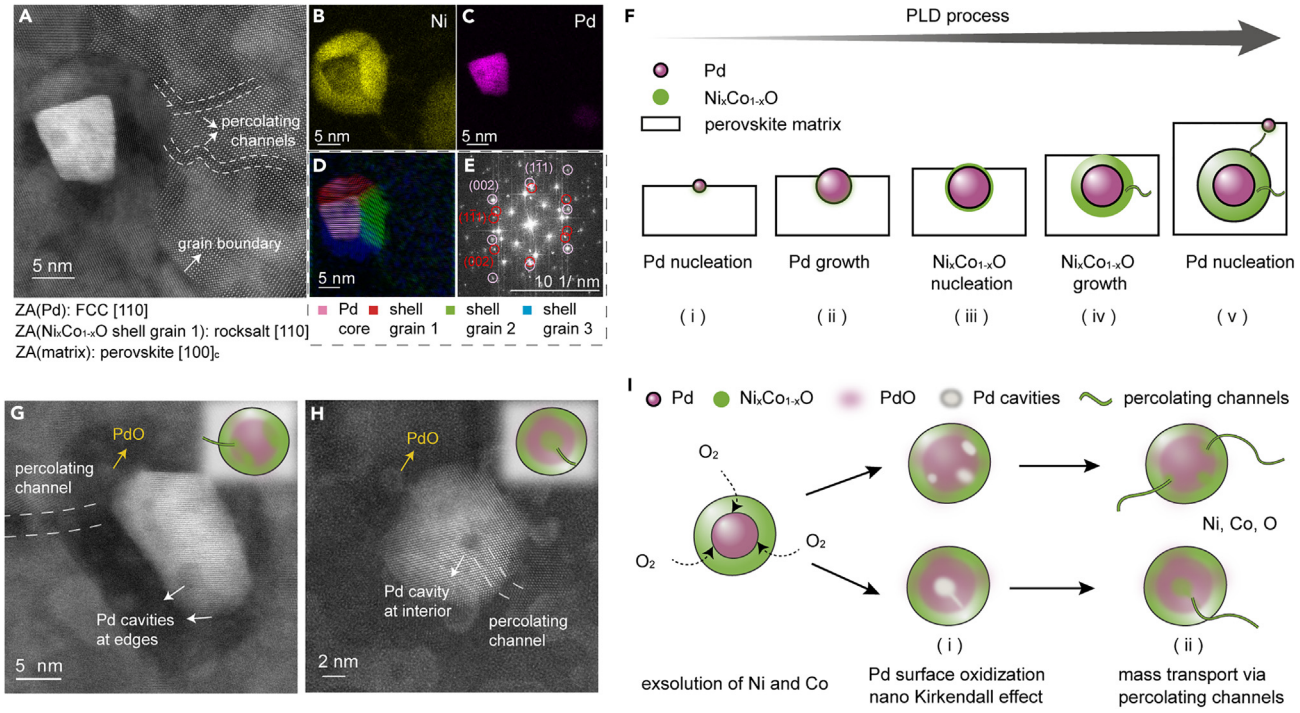

Figure 4. Phase identification and formation mechanism of core-shell Pd-$Ni_xCo_{1-x}O$ nanoparticles

(A) STEM HAADF image of a Pd-$Ni_xCo_{1-x}O$ core-shell nanoparticle embedded in a GB of the perovskite matrix, where the matrix is along perovskite $[100]_c$ zone axis (ZA) and the Pd core is along FCC [110] ZA.

(B and C) Corresponding STEM EDS mapping of Ni (B) and Pd (C).

(D) IFFT composite of Pd core (pink) and rock salt $Ni_xCo_{1-x}O$ shell grains in (A). The shell is composed of 3 grains marked as shell grain 1 (red), 2 (green), and 3 (blue). The shell grains nucleate and grow coherently at different facets of the Pd core.

(E) Composite FFT patterns of shell grain 1 (red) and Pd core (pink), showing $Ni_xCo_{1-x}O$ shell epitaxially grows along Pd surface.

(F) Formation mechanism of Pd-$Ni_xCo_{1-x}O$ core-shell nanoparticles: Pd nucleation (i) and growth (ii); Pd seeds exsolution of Ni and Co and nucleation of $Ni_xCo_{1-x}O$ at surface of Pd core (iii) and $Ni_xCo_{1-x}O$ grow to form a shell by mass transport by percolating channels (iv). A new Pd nucleus forms on the surface, initiating another core-shell particle (v).

(G and H) STEM HAADF images of self-assembled Pd-$Ni_xCo_{1-x}O$ core-shell nanoparticles showing cavities at the edge (G) and interior of Pd cores (H). These inverse-core-shell structures are filled with $Ni_xCo_{1-x}O$ and connected by percolating channels, as shown in the schematic inset.

(I) Mechanism of inverse core-shell structure: Pd cavities arise from nano-Kirkendall effect induced by local surface oxidation of Pd during exsolution of Ni and Co. $Ni_xCo_{1-x}O$ grows inside Pd cavities via diffusion along percolating channels.

analysis, confirming that self-assembled core-shell nanoparticles consist of a Pd metal core with a rock salt $Ni_xCo_{1-x}O$ shell. The shell Ni:Co ratio ranges from 1.5 to 1.9 (1.7 average) in 7 core-shell nanoparticles, indicating that the shell is a Ni-rich rock salt $Ni_{0.63}Co_{0.37}O$ (Figure S26; Note S15).

The 3D core-shell nanoparticle reconstruction and chemical composition analysis by APT confirm that Pd-$Ni_xCo_{1-x}O$ core-shell nanostructures are interconnected with percolating channels (Figures 5A–5C and S8; Videos S1, S2, S3, S4, S5, S6, and S7). Both APT tomography (Figures 5A–5C and S8) and STEM EDS mapping (Figure S13) illustrate that percolating channels are composed of Co, Ni, and O. Although percolating channels show similar chemical composition with $Ni_xCo_{1-x}O$ shells, the atomic structure was not resolved. Based on prior perovskite reduction studies yielding Fe exsolution,[11,27] Co-rich CoO_4 ordered sublayers[33] and Ruddlesden-Popper domain boundaries,[27] we infer that percolating channels are Ni- and Co-rich transition sublayers[33] and serve as mass transport pathways from matrix to $Ni_xCo_{1-x}O$ shell.[33] APT 3D reconstruction (Figure 5D) shows La_2O_3 next to the nanoparticle, which is consistent with FFT analysis (Figures S9F, S9J, and

Please cite this article in press as: Guo et al., Designing nanostructure exsolution-self-assembly in a complex concentrated oxide, Matter (2023), https://doi.org/10.1016/j.matt.2023.12.012

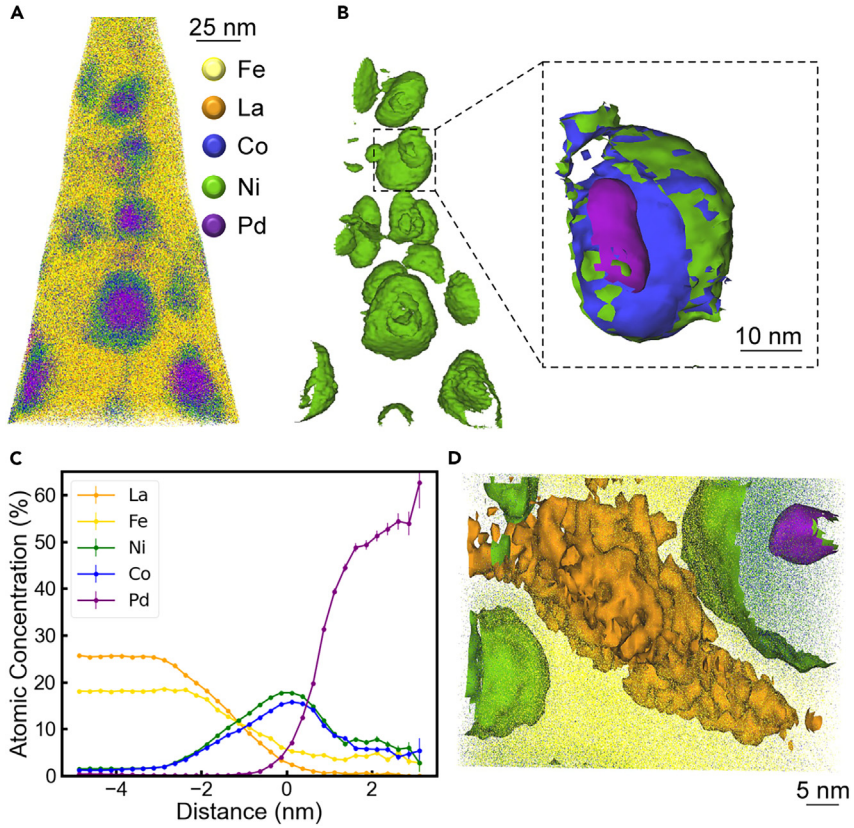

Figure 5. APT reconstruction of exsolution-self-assembled Pd-$Ni_xCo_{1-x}O$ core-shell nanoparticles interconnected by percolating channels

(A) Pd-$Ni_xCo_{1-x}O$ core-shell nanoparticles in Fe-rich perovskite matrix. Ni- and Co-rich channels are visible as blue-green filaments connecting the nanoparticles.

(B) Ni isosurface of Pd-$Ni_xCo_{1-x}O$ core-shell nanoparticles in (A) with the matrix removed to better reveal their 3D structure. An isolated core-shell particle with Ni (green), Co (blue), and Pd (purple) isosurfaces is shown in the expanded view.

(C) Atomic concentrations of relevant elements along the surface normal of a Pd isosurface. The Pd isosurface at zero distance is shown inset in (B).

(D) APT 3D reconstruction of secondary phase La_2O_3 showing its association with the core-shell nanoparticle.

S12A–S12I; Note S7) and STEM EDS mapping (Figures 2F, S9B, S12J, and S12K). Compared with the film deposited at 0.15 mTorr, in which no La_2O_3 phase is observed, La_2O_3 in the thin film deposited at 0.015 mTorr illustrates that the exsolution of Ni and Co promote local degradation of the perovskite phase associated with A-site separation.[34] In addition, the association of the secondary phase La_2O_3 with an adjacent core-shell nanostructure indicates that exsolution of $Ni_xCo_{1-x}O$ takes place around self-assembled Pd.

Tunable mixed-valence structure and its role in electrical transport

To understand the effect of nanostructure formation on material properties, electrical conductivity measurements identified the conduction mechanism as n-type electronic transport by small polaron hopping (Figure 6B). Importantly for potential applications, electronic conductivity values are tunable via P_{O_2} from 0.1 to 10 S/cm, and in line with the most-conductive $LaFeO_3$-type materials reported. Temperature-dependent cyclic voltammetry (CV) measurements enabled the calculation of conductivity activation energies (E_a) ranging from 79 to 232 meV (Figures S23 and

Please cite this article in press as: Guo et al., Designing nanostructure exsolution-self-assembly in a complex concentrated oxide, Matter (2023), https://doi.org/10.1016/j.matt.2023.12.012

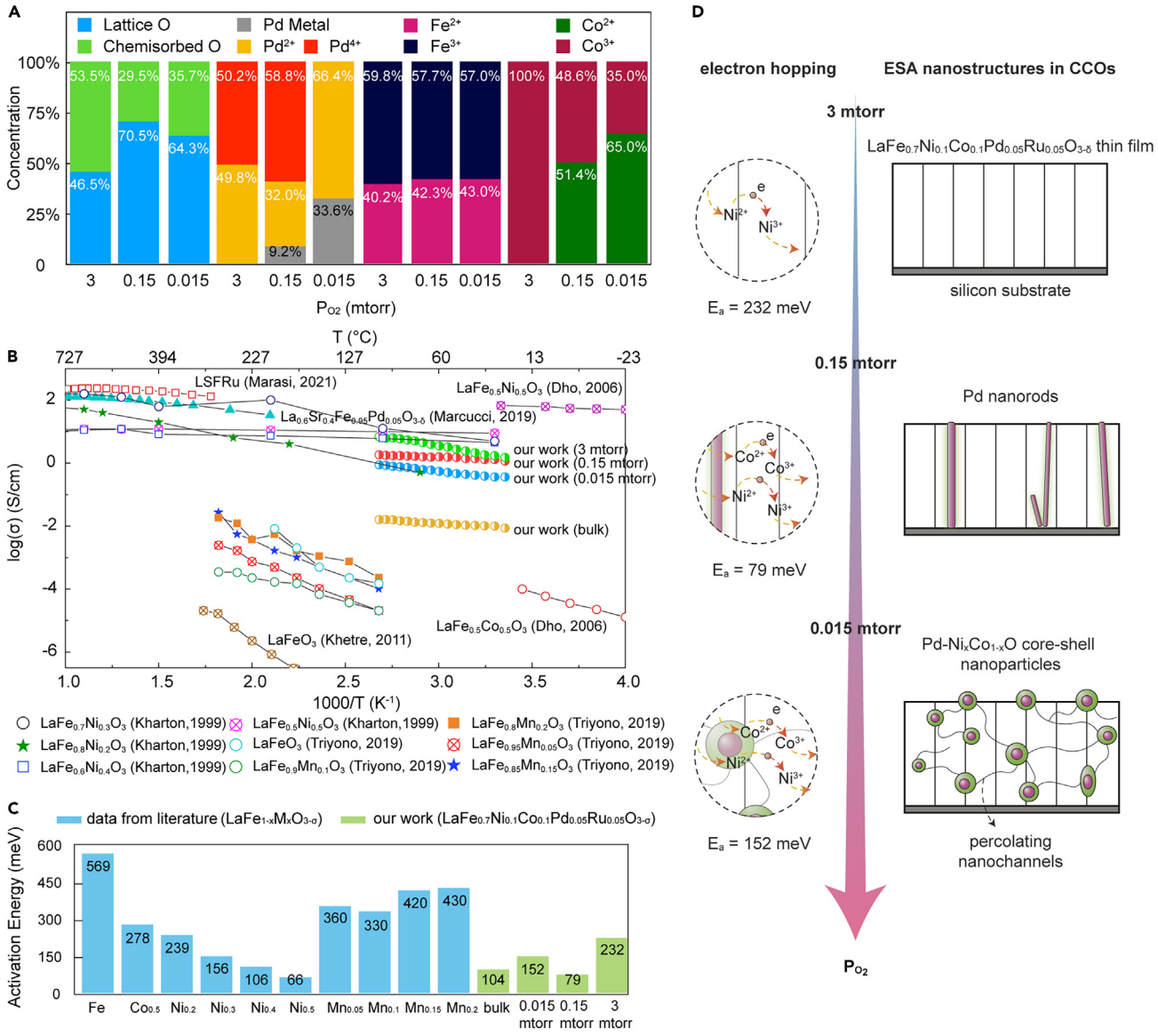

Figure 6. Tunable mixed-valence structure and its role in polaron hopping electronic transport

(A) XPS quantitative analysis of valence states of B-site cations and oxygen species in thin films deposited at different P_{O_2}.

(B and C) Electronic conductivity as function of temperature (B) and activation energy, E_a (C), of bulk PLD precursor and thin films, with comparison to typical $LaFeO_3$-based perovskites in the literature (Table S3).

(D) Influence of P_{O_2} on mixed-valence structure of thin films to modulate E_a of electronic conductivity.

S24; Tables S4 and S5; Notes S12 and S13), similar to expected values for Co- and Ni-facilitated polaron hopping in B-site substituted $LaFeO_3$-type materials (Figure 6C; Table S4).[35–40] The importance of the mixed-valence structure of cations (i.e., their content and distribution)[41] is apparent by the fact that the conductivity of the CCO films decreases with decreasing P_{O_2}.

Thus, XPS was used to quantify the cation valence state in the films, which is tunable via P_{O_2} due to the binding of $V_O^{\cdot\cdot}$ to reduced cations in the matrix lattice and nanostructure formation (Figures 6A and S17–S19; Table S3; Note S10). Given the extensive Pd nanostructure formation, contributions of Pd^{2+} and Pd^0 increase with

Please cite this article in press as: Guo et al., Designing nanostructure exsolution-self-assembly in a complex concentrated oxide, Matter (2023), https://doi.org/10.1016/j.matt.2023.12.012

decreasing P_{O_2} (increasing $V_O^{\cdot\cdot}$). Fe valence is nearly insensitive to $V_O^{\cdot\cdot}$ concentration given its lower reducibility than Co and Ni.[42] Co valence is highly sensitive to P_{O_2}, because Co^{2+} usually accompanies $V_O^{\cdot\cdot}$ formation for electroneutrality,[43] with the Co^{2+} concentration here increasing from 0% to 65% as P_{O_2} decreased from 3 to 0.015 mTorr. Although it is difficult to quantify Ni valence due to peak overlap of Ni $2p^{3/2}$ with La $3d^{3/2}$[44] in XPS (Note S14), qualitative XPS analysis shows mixed Ni^{2+}/Ni^{3+} in the 3 mTorr film, corresponding well with the fact that Ni is more reducible than Co[42] (Figure S25).

In addition to XPS, the distribution of Co and Ni mixed valency was probed by spatially resolved STEM EELS of a Pd nanorod and core-shell nanostructure, revealing increased amounts of Co^{2+} and Ni^{2+} surrounding the nanostructures (Figures S20 and S22; Note S11). This indicates that self-assembled Pd triggers Co^{3+} and Ni^{3+} reduction as part of the formation mechanism by a seed effect that is discussed below.

DISCUSSION

As demonstrated, ESA yields tunable nanostructures spontaneously in one self-assembly step, while allowing the cation exsolution sequence to be predicted by relative reducibility,[17] highlighting the power of the chemical complexity of CCOs to create diverse and unique nanocomposite materials. In this case, lowering P_{O_2} causes strongly reducible Pd to take electrons from lattice oxygen during reduction to Pd metal, releasing oxygen (Equation 1). Co and Ni with relatively weak reducibility may also take electrons from lattice oxygen to reach a reduced valence state, but they form a thermodynamically stable suboxide phase instead of further reduction to metal (e.g., Equation 2).[12]

$$O_O^{\times} + Pd_{Pd}^{\times} \rightarrow V_O^{\cdot\cdot} + V_{Pd}'' + Pd + \frac{1}{2}O_{2\,(g)} \qquad \text{(Equation 1)}$$

$$3\,O_O^{\times} + 2\,Co_{Co}^{\times} \rightarrow 3\,V_O^{\cdot\cdot} + 2\,V_{Co}''' + 2\,CoO + \frac{1}{2}O_{2\,(g)} \qquad \text{(Equation 2)}$$

As mentioned above, Ni/Co-coated Pd nanorods are self-assembled by a variant of a previously identified mechanism[15]; however, we observed an intricate core-shell nanostructure growth mechanism that relies on sequential Pd metal phase formation, which seeds the mixed-oxide shell growth and whose constituents use percolating mass transport channels. Recalling that the $Ni_xCo_{1-x}O$ shell is polycrystalline (Figures 4D, S9K–S9N, and S10) and each $Ni_xCo_{1-x}O$ grain shows an epitaxial relation with its corresponding Pd core surface (Figures 4E and S10), it is hypothesized that Ni and Co exsolution and nucleation and growth of $Ni_xCo_{1-x}O$ are triggered by Pd cores via a seed effect[45] (Figure 6F; Note S6). Following Figure 4F, during PLD, (i) exsolved Pd crystals nucleate on the surface of the film; (ii) additional Pd diffuses to and coarsens the nuclei; (iii) Pd crystals seed the self-assembly of reduced Co and Ni due to the Pd–matrix interfacial stress effect (see GPA; Note S5); (iv) $Ni_xCo_{1-x}O$ phase thickens around the Pd to form a shell via diffusion of Ni and Co along percolating channels; and (v) Pd core growth is restricted by $Ni_xCo_{1-x}O$ shell and nanostructure growth is confined by the CCO matrix, causing new Pd nuclei on the surface and generating new core-shell nanoparticles via repeating steps (ii)–(v). Interestingly, cavities appear at both edges and interiors of Pd metal cores (Figures 4G, 4H, S11, and S14; Note S9), supporting the hypothesis that cavities in the Pd metal arise from the nano-Kirkendall effect[46] induced by local surface oxidation of Pd by O_2 released from lattice oxygen during exsolution[47] of Ni and Co (Figure 4I; Note S9). During surface oxidation, Pd vacancies form in the metal due to their faster

Please cite this article in press as: Guo et al., Designing nanostructure exsolution-self-assembly in a complex concentrated oxide, Matter (2023), https://doi.org/10.1016/j.matt.2023.12.012

outward diffusivity compared to the inward diffusivity of O, generating Pd-depleted cavities that merge at the surfaces and interior of Pd cores (Figure 4I(i)). This allows self-assembling $Ni_xCo_{1-x}O$ growth within cavities, again via percolating channels (Figures 4I(ii), S15, and S16).

Lastly, interpretation of the correlation of electronic transport with nanostructure formation considers their effects on the CCO perovskite matrix, whose mixed-valence cation network needed for polaron hopping is strongly affected by ESA (Figure 6D). $LaFeO_3$-based perovskites facilitate small polaron hopping (Note S12), but given the recent emergence of CCOs, HEOs, and ESOs, their electronic (and generally electrical) transport mechanisms are not well understood because they depend on interrelated factors such as the concentration and type of elements present, amount and type of disorder, and spin states.[2] Hence, the interpretation of electronic conductivity and activation energy focuses on three aspects: cation mixed valence, cation site occupancy/vacancy, and secondary phases. Mixed-valence cation pairs facilitate polaron hopping, and decreasing their separation decreases the activation energy for polaron conduction by increasing electron wavefunction and orbital overlap.[48] Cation vacancies lower the concentration of hopping sites, and thus absolute conductivity value, without affecting the relative amounts of mixed-valence pairs (i.e., without affecting the activation energy). Secondary phases, concomitant with cation vacancies, decrease the total volume of the polaron conducting phase. As detailed in Note S12, the low conductivity (~10 mS/cm) of the ceramic PLD precursor is attributed to insulating La_2O_3 secondary phases, and the sparse network of B-site cation mixed valency they induce. We believe it is feasible to mitigate the formation of La_2O_3 and propose several design strategies regarding CCO targets and PLD growth conditions (Note S17).

All thin films have higher conductivity than the precursor, although their conductivities decrease with decreasing P_{O_2} (i.e., increasing $V_O^{\cdot\cdot}$ concentration), suggesting a complex electronic transport mechanism that is sensitive to nanostructure formation and cation mixed valency (Figure 6D). Ru surface accumulation is expected to produce ~5% B-site vacancies ($V_{Ru}^{//}$) compensated by $V_O^{\cdot\cdot}$ in the matrix. The 3-mTorr film is the only single-phase sample (Figures 1 and S1) and is the most conductive despite also having the highest E_a of 232 meV (Figures 6B and 6C), which, given no XPS or EELS evidence for Co^{2+}/Co^{3+} mixed valency, is attributed to Ni^{2+}/Ni^{3+}-facilitated polaron hopping (Figures 6A, S20, and S21; Note S11). The 0.15-mTorr film has Pd nanorods with Ni- and Co-enriched nanorod–matrix interfaces (Figures 2H, 2K, and S7) and lower conductivity and E_a (79 meV) than the 3-mTorr film (Figures 6B and 6C); lower E_a is attributed to increased Co^{2+} concentration, which decreases the Co, and presumably Ni, small polaron pair separation,[48] and approaches that of 50% Ni-substituted $LaFeO_3$ (66 meV).[35] The 0.015-mTorr film contains connected Pd-$Ni_xCo_{1-x}O$ core-shells and La_2O_3 volumes; compared to the 0.15-mTorr film, insulating La_2O_3 lowers conductivity, whereas higher E_a (152 meV) is attributed to the further increased Co^{2+} concentration that widens Co and Ni small polaron pair separation and thus E_a,[48] which is comparable to 30% Ni-doped $LaFeO_3$ (E_a = 156 meV).[35] It is also hypothesized that $V_O^{\cdot\cdot}$ causes strong electron localization at a subset of cations (e.g., Fe[49]), which halts charge transport near these cation-vacancy associates.[49,50] This reduces the total percolating volume for current carriers (via other mixed-valence cations, e.g., Co and Ni), leading to a more tortuous conduction pathway and lower conductivity.

In summary, we demonstrated tunable nanostructure growth in a CCO by a simple method: ESA. ESA is a one-step approach to direct the evolution of nanoparticles

Please cite this article in press as: Guo et al., Designing nanostructure exsolution-self-assembly in a complex concentrated oxide, Matter (2023), https://doi.org/10.1016/j.matt.2023.12.012

and nanorods in CCO-derived composites in a perovskite $LaFeO_3$-inspired model CCO, and we present a case study demonstrating how to simply access different nanostructures via the control of oxygen partial pressure. This synthetic approach is expected to be generally applicable to various substrate materials and device architectures as suggested through successful growth on multiple crystalline and amorphous oxide and metal substrates here. A detailed examination of $LaFe_{0.7}Ni_{0.1}Co_{0.1}Pd_{0.05}Ru_{0.05}O_{3-\delta}$ CCO thin films with atomic-scale electron- and atom-probe imaging and spectroscopies revealed that ESA can be directed using Ellingham's model of cation reducibility, and mass transport via extended defects governs local morphology formation. Furthermore, ESA enables the tailored growth of novel multielement nanorod and nanoparticle composite structures whose formation is correlated with the electronic conductivity of films, which exceeds 0.1 S/cm at room temperature. Given the vast combinatorial space of CCOs, which includes HEOs and ESOs, ESA is expected to be highly extensible via the integration of novel compositions and crystal structures.

EXPERIMENTAL PROCEDURES

Resource availability

Lead contact

Further information and requests for resources and reagents should be directed to and will be fulfilled by the lead contact, William J. Bowman (will.bowman@uci.edu).

Materials availability

Materials generated in this study will be made available on request, but we may require a payment and/or a completed materials transfer agreement if there is potential for commercial application.

Data and code availability

The data generated and analyzed in this study are available from the corresponding author on reasonable request. This paper does not report original code. Any additional information required to reanalyze the data reported in this paper is available from the lead contact upon request.

Sample preparation

The CCO powders were prepared with a method derived from the Pechini method. Nitrate salts of the constituent metals were mixed in stoichiometric ratios and dissolved in water. Citric acid (3 mol/mol perovskite) and ethylene glycol butyl ether (1 mol/mol perovskite) were subsequently added while the solution was being stirred and heated at 60°C. The solution was dried overnight at 110°C, which resulted in xerogel formation. The xerogel was ground finely in a mortar and pestle and then calcined in a muffle furnace at 800°C for 4 h.

The prepared CCO powders were uniaxially pressed (Strongway 20-Ton Hydraulic Shop Press) at 100 MPa and then followed by cold-isostatic compress (EQ-CIP20-DIE, MTI Corporation) at 200 MPa to make a PLD precursor target pellet. The pellet was sintered at 1,200°C for 12 h in air with a ramp rate of 10°C/min in a tube furnace (Carbolite Gero CC-T1).

Thin films were fabricated using PLD with an Nd:YAG solid laser (Continuum SL III-10, 266-nm wavelength, 10-ns pulse duration) in a high-vacuum deposition system (Neocera Pioneer 180 GLAD PLD System). Silicon (100) single crystal substrates (MTI Corporation) are ultrasonically cleaned in acetone, isopropanol, and methanol

Please cite this article in press as: Guo et al., Designing nanostructure exsolution-self-assembly in a complex concentrated oxide, Matter (2023), https://doi.org/10.1016/j.matt.2023.12.012

before PLD. The cleaned substrates are fixed at the center of the substrate holder with the substrate-target distance of 57 mm. During PLD, 30,000 laser pulses with an energy fluence of 5.3 J/cm^2 and a laser frequency of 5 Hz were applied to the PLD target to produce a plasma plume deposited on the silicon substrate with a surface temperature of 650°C. We chose this temperature based on prior work showing high crystallinity and density.[51] Mass flow of high-purity O_2 (99.994%) and turbomolecular pump speed were used to tune P_{O_2} during PLD.

Characterization

The crystal structure and lattice distortion of the prepared thin films and the CCO PLD target were examined by XRD (Rigaku SmartLab set to 40 kV and 44 mA) in a symmetric θ-2θ configuration using Cu $K_{\alpha 1}$ radiation (1.54 Å wavelength). The XRD of thin films was operated in general parallel beam/parallel slit analyzer mode with 0D detector, whereas the XRD of the target pellet was conducted in general Bragg-Brentano mode with a 1D detector. Thin film surface morphology was observed with SEM (TESCAN GAIA-3 XHM field-emission SEM [FESEM]) operated at 7 kV with a work distance of 5 mm. The sample surface was sputtered with 5 nm Ir to avoid charging (EMS 150T sputter coater).

STEM specimens were prepared by focused ion beam (FIB) operated at 30 kV for trenching and at 15 or 3 kV for thinning (TESCAN GAIA-3 XHM FESEM). Thin films morphology, phase identification, chemical composition, and local electronic structure were characterized by STEM EDS and EELS using JEOL Grand ARM300CF, equipped with dual 100-mm^2 silicon drift detectors and Gatan GIF Quantum K2. Data acquisition and processing, including GPA and FFT analysis, have been conducted in Gatan Microscopy Suite (GMS 3).

Cation valence states and oxygen species of the prepared thin films were derived and analyzed by XPS carried out using a Kratos AXIS-Supra instrument with a monochromatic Al K_α X-ray source. The high-resolution XPS spectra for C1s, O1s, La 3d, Fe 2p, Co 2p, Ni 2p, Pd 3d, and Ru 3d were recorded. The binding energies of all of the spectra were calibrated by standard C1s peak at 284.8 eV for charging effect correction. Peak components of the acquired XPS spectra were analyzed quantitatively using CasaXPS software.

To prepare samples for APT analysis, portions of the TEM specimens were welded onto Si microposts and sharpened by annular milling in an FEI Helios dual-beam FIB microscope. APT was performed with a local-electrode atom-probe (LEAP) 5000 XS (Cameca) at a sample temperature of 30 K and a background pressure of 5×10^{-11} Torr. A 355-nm ultraviolet laser was used to evaporate the sample at a pulse rate of 250 kHz and a pulse energy of 22 pJ. IVAS 3.8.6 was used to reconstruct the data and provide a 3D composition profile.

Electrical transport measurements

Several 30-nm Ir contacts were deposited onto the surface of the thin films as electrodes via sputtering (EMS 150T sputter coater). In-plane CV tests were carried out using a Biologic sp-200 electrochemical workstation associated with Linkam probe stage (HFS600E-PB4) and Linkam temperature controller (T96 System Controller) for measuring electronic conductivity and deriving activation energy for polaron hopping (Figure S19). Out-of-plane CV tests were conducted for measuring electronic conductivity of the PLD target in which silver ink (Fuel Cell Materials, Nexceris) was coated on both sides as electrodes.

Please cite this article in press as: Guo et al., Designing nanostructure exsolution-self-assembly in a complex concentrated oxide, Matter (2023), https://doi.org/10.1016/j.matt.2023.12.012

SUPPLEMENTAL INFORMATION

Supplemental information can be found online at https://doi.org/10.1016/j.matt.2023.12.012.

ACKNOWLEDGMENTS

W.J.B. thanks the University of California (UC) Irvine School of Engineering new faculty set-up funds. H.G. and W.J.B. acknowledge financial support from the American Chemical Society's Petroleum Research Fund Doctoral New Investigator Grant PRF 61961-DNI. M.B., H.G., J.D.S., and W.J.B. acknowledge funding under the award National Science Foundation (NSF) CAREER DMR-2042638. X.W. and W.J.B. acknowledge partial support from funding by the NSF Materials Research Science and Engineering Center (MRSEC) program through the UC Irvine Center for Complex and Active Materials (CCAM DMR-2011967). S.S. and K.L.G.-A. acknowledge primary support from funding by the NSF MRSEC Seed program through the UC Irvine Center for Complex and Active Materials (DMR-2011967). For XRD, STEM-EDS/EELS, and XPS characterization, the authors acknowledge the use of facilities and instrumentation at the UC Irvine Materials Research Institute (IMRI), supported in part by the NSF MRSEC program through the UC Irvine CCAM (DMR-2011967). The authors are grateful to Dr. Qiyin Lin at the UC IMRI for technical assistance with XRD characterization. L.J.L. and C.M. acknowledge partial support from the NSF MRSEC (DMR-1720139). APT was performed at the Northwestern University Center for Atom-Probe Tomography (NUCAPT). The LEAP tomograph at NUCAPT was purchased and upgraded with grants from the NSF-MRI (DMR-0420532) and ONR-DURIP (N00014-0400798, N00014-0610539, N00014-0910781, and N00014-1712870) programs. NUCAPT received support from the MRSEC program (NSF DMR-1720139) at the Materials Research Center, the Soft and Hybrid Nanotechnology Experimental (SHyNE) Resource (NSF ECCS-2025633), and the Initiative for Sustainability and Energy at Northwestern University. This work made use of the EPIC facility of the NUANCE Center at Northwestern University, which has received support from the SHyNE Resource (NSF ECCS-1542205), the MRSEC program (NSF DMR-1720139) at the Materials Research Center, the International Institute for Nanotechnology (IIN), the Keck Foundation, and the State of Illinois, through the IIN.

AUTHOR CONTRIBUTIONS

H.G. and W.J.B. conceived and designed this research. S.S. prepared the CCO powder under the supervision of K.L.G.-A. H.G. fabricated the CCO PLD target, prepared the thin films, and performed XRD and SEM characterization. H.G. and X.W. prepared TEM samples with FIB. H.G., X.W., M.X., and T.A. performed the STEM-EDS and EELS characterization. H.G. and M.X. conducted the STEM GPA. C.M. performed APT analysis under the supervision of L.J.L. I.T. and H.G. performed the XPS experiments. M.B. conducted the CV tests. J.D.S. performed statistics on self-assembled nanophases. H.G., C.M., M.B., and W.J.B. interpreted the characterization and property data. H.G. wrote the manuscript. All coauthors commented on the manuscript and contributed to the final revision. W.J.B. supervised the study.

DECLARATION OF INTERESTS

The authors declare no competing interests.

Received: August 3, 2023
Revised: October 17, 2023
Accepted: December 11, 2023
Published: January 11, 2024

REFERENCES

1. Rost, C.M., Sachet, E., Borman, T., Moballegh, A., Dickey, E.C., Hou, D., Jones, J.L., Curtarolo, S., and Maria, J.-P. (2015). Entropy-stabilized oxides. Nat. Commun. *6*, 8485.
2. Brahlek, M., Gazda, M., Keppens, V., Mazza, A.R., McCormack, S.J., Mielewczyk-Gryń, A., Musico, B., Page, K., Rost, C.M., Sinnott, S.B., et al. (2022). What is in a name: Defining "high entropy" oxides. Apl. Mater. *10*, 110902.
3. Zeng, Y., Ouyang, B., Liu, J., Byeon, Y.-W., Cai, Z., Miara, L.J., Wang, Y., and Ceder, G. (2022). High-entropy mechanism to boost ionic conductivity. Science *378*, 1320–1324.
4. Zhang, R., Wang, C., Zou, P., Lin, R., Ma, L., Yin, L., Li, T., Xu, W., Jia, H., Li, Q., et al. (2022). Compositionally complex doping for zero-strain zero-cobalt layered cathodes. Nature *610*, 67–73.
5. Misra, S., and Wang, H. (2021). Review on the growth, properties and applications of self-assembled oxide–metal vertically aligned nanocomposite thin films—current and future perspectives. Mater. Horiz. *8*, 869–884.
6. Huang, J., Li, W., Yang, H., and MacManus-Driscoll, J.L. (2021). Tailoring physical functionalities of complex oxides by vertically aligned nanocomposite thin-film design. MRS Bull. *46*, 159–167.
7. Neagu, D., Tsekouras, G., Miller, D.N., Ménard, H., and Irvine, J.T.S. (2013). In situ growth of nanoparticles through control of non-stoichiometry. Nat. Chem. *5*, 916–923.
8. Zhu, T., Troiani, H.E., Mogni, L.V., Han, M., and Barnett, S.A. (2018). Ni-Substituted Sr(Ti,Fe)O3 SOFC Anodes: Achieving High Performance via Metal Alloy Nanoparticle Exsolution. Joule *2*, 478–496.
9. Kwon, O., Joo, S., Choi, S., Sengodan, S., and Kim, G. (2020). Review on exsolution and its driving forces in perovskites. JPhys Energy *2*, 032001.
10. Kousi, K., Tang, C., Metcalfe, I.S., and Neagu, D. (2021). Emergence and Future of Exsolved Materials. Small *17*, 2006479.
11. Wang, J., Syed, K., Ning, S., Waluyo, I., Hunt, A., Crumlin, E.J., Opitz, A.K., Ross, C.A., Bowman, W.J., and Yildiz, B. (2022). Exsolution Synthesis of Nanocomposite Perovskites with Tunable Electrical and Magnetic Properties. Adv. Funct. Mater. *32*, 2108005.
12. Buharon, M., Singh, S., Komarala, E.P., and Rosen, B.A. (2018). Expanding possibilities for solid-phase crystallization by exsolving tunable Pd–NiO core–shell nanostructures. CrystEngComm *20*, 6372–6376.
13. Shah, S., Xu, M., Pan, X., and Gilliard-AbdulAziz, K.L. (2022). Complex Alloy and Heterostructure Nanoparticles Derived from Perovskite Oxide Precursors for Catalytic Dry Methane Reforming. ACS Appl. Nano Mater. *5*, 17476–17481.
14. Wang, J., Kumar, A., Wardini, J.L., Zhang, Z., Zhou, H., Crumlin, E.J., Sadowski, J.T., Woller, K.B., Bowman, W.J., LeBeau, J.M., and Yildiz, B. (2022). Exsolution-Driven Surface Transformation in the Host Oxide. Nano Lett. *22*, 5401–5408.
15. Chen, A., and Jia, Q. (2021). A pathway to desired functionalities in vertically aligned nanocomposites and related architectures. MRS Bull. *46*, 115–122.
16. Kawasaki, S., Takahashi, R., Yamamoto, T., Kobayashi, M., Kumigashira, H., Yoshinobu, J., Komori, F., Kudo, A., and Lippmaa, M. (2016). Photoelectrochemical water splitting enhanced by self-assembled metal nanopillars embedded in an oxide semiconductor photoelectrode. Nat. Commun. *7*, 11818.
17. (1944). Transactions and Communications. J. Soc. Chem. Ind. *63*, 125–160.
18. Kwon, O., Sengodan, S., Kim, K., Kim, G., Jeong, H.Y., Shin, J., Ju, Y.-W., Han, J.W., and Kim, G. (2017). Exsolution trends and co-segregation aspects of self-grown catalyst nanoparticles in perovskites. Nat. Commun. *8*, 15967.
19. Ren, K., Zhang, L., Miao, J., Zhao, J., Yang, S., Fu, Y., Li, Y., and Han, S. (2022). Boosting the high-temperature discharge performance of nickel-hydrogen batteries based on perovskite oxide Co-coated LaFeO3 as proton insertion anode. Int. J. Hydrogen Energy *47*, 14961–14970.
20. Ma, Z., Zhou, J., Li, Y., Liu, C., Pu, J., and Chen, X. (2020). Developments in CO2 Electrolysis of Solid Oxide Electrolysis Cell with Different Cathodes. Fuel Cell. *20*, 650–660.
21. Li, J., Luo, W., Wang, X., Yu, C., Zhang, Y., and Meng, F. (2022). Preparation and research of high-performance LaFeO3/RGO supercapacitor. J. Solid State Electrochem. *26*, 1291–1301.
22. Pidburtnyi, M., Zanca, B., Coppex, C., Jimenez-Villegas, S., and Thangadurai, V. (2021). A Review on Perovskite-Type LaFeO3 Based Electrodes for CO2 Reduction in Solid Oxide Electrolysis Cells: Current Understanding of Structure–Functional Property Relationships. Chem. Mater. *33*, 4249–4268.
23. Manzoor, S., Husain, S., Somvanshi, A., Fatema, M., and Zarrin, N. (2019). Exploring the role of Zn doping on the structure, morphology, and optical properties of LaFeO3. Appl. Phys. A *125*, 509.
24. Ren, K., Miao, J., Shen, W., Su, H., Pan, Y., Zhao, J., Pan, X., Li, Y., Fu, Y., Zhang, L., and Han, S. (2022). High temperature electrochemical discharge performance of LaFeO3 coated with C/Ni as anode material for NiMH batteries. Prog. Nat. Sci.: Mater. Int. *32*, 684–692.
25. Chen, X.Y., Zhang, L.H., Wang, Y.P., Wu, S.Q., Hou, Z.F., and Zhu, Z.Z. (2021). First-Principles Studies on the Formation of Oxygen Vacancies in Li2CoSiO4. J. Electrochem. Soc. *168*, 110527.
26. Liu, B., Aidhy, D.S., Zhang, Y., and Weber, W.J. (2014). Theoretical investigation of thermodynamic stability and mobility of the oxygen vacancy in ThO2–UO2 solid solutions. Phys. Chem. Chem. Phys. *16*, 25461–25467.
27. Syed, K., Wang, J., Yildiz, B., and Bowman, W.J. (2022). Bulk and surface exsolution produces a variety of Fe-rich and Fe-depleted ellipsoidal nanostructures in La0.6Sr0.4FeO3 thin films. Nanoscale *14*, 663–674.
28. Wang, Z., Liu, B., and Lin, J. (2013). Highly effective perovskite-type BaZrO3 supported Ru catalyst for ammonia synthesis. Appl. Catal. Gen. *458*, 130–136.
29. Basahel, S.N., Medkhali, A.H., Mokhtar, M., and Narasimharao, K. (2022). Noble metal (Pd, Pt and Rh) incorporated LaFeO3 perovskite oxides for catalytic oxidative cracking of n-propane. Catal. Today *397–399*, 81–93.
30. Wang, J., Yang, J., Opitz, A.K., Bowman, W., Bliem, R., Dimitrakopoulos, G., Nenning, A., Waluyo, I., Hunt, A., Gallet, J.-J., and Yildiz, B. (2021). Tuning Point Defects by Elastic Strain Modulates Nanoparticle Exsolution on Perovskite Oxides. Chem. Mater. *33*, 5021–5034.
31. Jauch, W., and Reehuis, M. (2002). Electron density distribution in paramagnetic and antiferromagnetic CoO: A \ensuremath {\gamma}-ray diffraction study. Phys. Rev. B *65*, 125111.
32. Kuo, T.Y., Chen, S.C., Peng, W.C., Lin, Y.C., and Lin, H.C. (2011). Influences of process parameters on texture and microstructure of NiO films. Thin Solid Films *519*, 4940–4943.
33. Li, J., Guan, M.-X., Nan, P.-F., Wang, J., Ge, B.-H., Qiao, K.-M., Zhang, H.-R., Liang, W.-H., Hao, J.-Z., Zhou, H.-B., et al. (2020). Topotactic phase transformations by concerted dual-ion migration of B-site cation and oxygen in multivalent cobaltite La–Sr–Co–Ox films. Nano Energy *78*, 105215.
34. Shah, S., Xu, M., Pan, X., and Gilliard-Abdulaziz, K.L. (2021). Exsolution of Embedded Ni–Fe–Co Nanoparticles: Implications for Dry Reforming of Methane. ACS Appl. Nano Mater. *4*, 8626–8636.
35. Kharton, V.V., Viskup, A.P., Naumovich, E.N., and Tikhonovich, V.N. (1999). Oxygen permeability of LaFe1−xNixO3−δ solid solutions. Mater. Res. Bull. *34*, 1311–1317.
36. Triyono, D., Laysandra, H., Liu, H.L., and Anugrah, A.W. (2019). Structural, optical, and dielectric properties of LaFe1−xMnxO3 (x = 0.00, 0.05, 0.10, 0.15, and 0.20) perovskites. J. Mater. Sci. Mater. Electron. *30*, 18584–18598.
37. Dho, J., and Hur, N.H. (2006). Magnetic and transport properties of lanthanum perovskites with B-site half doping. Solid State Commun. *138*, 152–156.
38. Marcucci, A., Zurlo, F., Sora, I.N., Placidi, E., Casciardi, S., Licoccia, S., and Di Bartolomeo, E. (2019). A redox stable Pd-doped perovskite for SOFC applications. J. Mater. Chem. A Mater. *7*, 5344–5352.
39. Marasi, M., Panunzi, A.P., Duranti, L., D'Ottavi, C., and Di Bartolomeo, E. (2021). Perovskites Doped with Small Amounts of Noble Metals for IT-SOFCs. ECS Trans. *103*, 2137–2144.
40. Khetre, S.M., Jadhav, H.V., Jagadale, P.N., Kulal, S.R., and Bamane, S.R. (2011). Studies on electrical and dielectric properties of LaFeO3. Adv. Appl. Sci. Res. *2*, 503–511.
41. Idrees, M., Nadeem, M., and Hassan, M.M. (2010). Investigation of conduction and relaxation phenomena in LaFe0.9Ni0.1O3 by

impedance spectroscopy. J. Phys. D Appl. Phys. *43*, 155401.

42. Wang, H., Dong, X., Zhao, T., Yu, H., and Li, M. (2019). Dry reforming of methane over bimetallic Ni-Co catalyst prepared from La(CoxNi1-x)0.5Fe0.5O3 perovskite precursor: Catalytic activity and coking resistance. Appl. Catal. B Environ. *245*, 302–313.

43. Wang, T., He, H., Meng, Z., Li, S., Xu, M., Liu, X., Zhang, Y., Liu, M., and Feng, M. (2022). Magnetic Field-Enhanced Electrocatalytic Oxygen Evolution on a Mixed-Valent Cobalt-Modulated LaCoO3 Catalyst. ChemPhysChem *24*, e202200845.

44. Yang, M., Huo, L., Zhao, H., Gao, S., and Rong, Z. (2009). Electrical properties and acetone-sensing characteristics of LaNi1−xTixO3 perovskite system prepared by amorphous citrate decomposition. Sensor. Actuator. B Chem. *143*, 111–118.

45. Jo, S., Han Kim, Y., Jeong, H., Park, C.-h., Won, B.-R., Jeon, H., Taek Lee, K., and Myung, J.-h. (2022). Exsolution of phase-separated nanoparticles via trigger effect toward reversible solid oxide cell. Appl. Energy *323*, 119615.

46. Mali, S.S., Patil, J.V., and Hong, C.K. (2020). Formation of Kirkendall void of lead-sulfide cubes. Mater. Today *40*, 266–267.

47. Cao, P., Tang, P., Bekheet, M.F., Du, H., Yang, L., Haug, L., Gili, A., Bischoff, B., Gurlo, A., Kunz, M., et al. (2022). Atomic-Scale Insights into Nickel Exsolution on LaNiO3 Catalysts via In Situ Electron Microscopy. J. Phys. Chem. C Nanomater. Interfaces *126*, 786–796.

48. Natanzon, Y., Azulay, A., and Amouyal, Y. (2020). Evaluation of Polaron Transport in Solids from First-principles. Isr. J. Chem. *60*, 768–786.

49. Das, T., Nicholas, J.D., and Qi, Y. (2017). Polaron size and shape effects on oxygen vacancy interactions in lanthanum strontium ferrite. J. Mater. Chem. A Mater. *5*, 25031–25043.

50. Eppstein, R., and Caspary Toroker, M. (2022). On the Interplay Between Oxygen Vacancies and Small Polarons in Manganese Iron Spinel Oxides. ACS Mater. Au *2*, 269–277.

51. Guo, H., Wang, X., Dupuy, A.D., Schoenung, J.M., and Bowman, W.J. (2022). Growth of nanoporous high-entropy oxide thin films by pulsed laser deposition. J. Mater. Res. *37*, 124–135.